International Journal of Fracture **85:** 381–402, 1997.

Dynamic crack growth across an interface

T. SIEGMUND[1], N.A. FLECK[2] and A. NEEDLEMAN[3]
[1] *Institute of Materials Research, GKSS Research Center, Geesthacht, FRG*
[2] *Engineering Department, Cambridge University, Cambridge, CB2 1PZ, England*
[3] *Division of Engineering, Brown University, Providence, RI, 02912 USA*

Received 11 February 1997; accepted in revised form 24 June 1997

Abstract. The growth of a crack first in an elastic solid, then across an interface and into an elastic-viscoplastic solid is analyzed numerically. The analyses are carried out within a framework where the continuum is characterized by two constitutive relations; one that relates stress and strain in the bulk material, the other relates the traction and separation across a specified set of cohesive surfaces. Crack initiation, crack growth and crack arrest emerge naturally as outcomes of the imposed loading, without any ad hoc assumptions concerning crack growth or crack path selection criteria. Full transient analyses are carried out using two characterizations of strain rate hardening for the viscoplastic solid; power law strain rate hardening and a combined power law-exponential relation that gives rise to enhanced strain rate hardening at high strain rates. Results are presented for two values of interface strength. For the higher strength interface the crack grows straight through the interface into the elastic–viscoplastic solid, while for the lower strength interface the crack deflects into the interface.

1. Introduction

A key issue for the toughness of multi-phase materials is whether a crack initiating in one phase will grow into the adjacent phase or will be deflected into the interface between them. In particular, a number of two phase materials are of interest where one of the phases remains elastic and is brittle, while the other phase is ductile and can deform plastically. Examples include metal-matrix composites, layered metal-ceramic materials and structural steels in which iron-carbide inclusions are the brittle phase.

The interaction between stationary cracks and interfaces, when the materials on each side of the interface are elastic has been analyzed in several investigations, e.g. Cook and Erdogan, (1972), Erdogan and Biricikoglu, (1975), Goree and Venezia, (1977), Lu and Erdogan, (1983) and He and Hutchinson, (1989). The effect of plastic flow on this interaction has recently been investigated by Sugimura et al. (1995). Of particular interest is the determination of the conditions under which a crack will propagate across an interface as opposed to when it will be deflected into the interface. This question has not previously been addressed for dynamically growing cracks. Dynamic effects, of course, need to be accounted for under impact loading conditions. However, dynamic effects can be important even under quasi-static loading conditions because cracks initiating in the brittle phase can attain high speeds before encountering the interface.

The contributions of plastic flow and interface strength to overall toughness are complex. Inelastic plastic deformation of metallic fibers or layers may have only a moderate effect on the toughness since the metal layer is constrained between elastic layers. Hence, the degree of plastic straining and energy absorption are limited. For example, Ashby et al. (1989) have examined the contribution to crack work from bridging of a ceramic matrix by metallic fibers. They found that well-bonded fibers provide large crack bridging stresses (3–5 times the flow strength of the metal fiber) but low ductility, and low overall toughness.

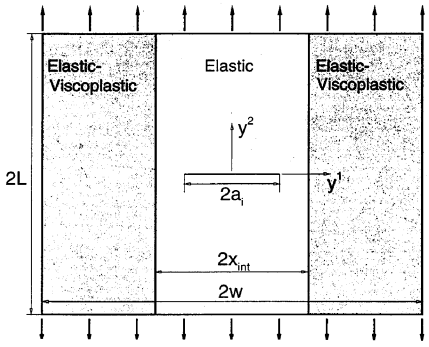

Figure 1. Geometry of the center cracked bimaterial specimen.

A poorly bonded interface between fiber and matrix results in smaller bridging stresses but much larger elongation to failure of the metallic fibers bridging the crack and thereby to greater toughness. As another example, Shaw et al. (1996) have explored ways of toughening ceramics by adding sandwich metallic layers transverse to the plane of a crack, with the interfacial strength sufficiently high for the crack not to deflect along the interface between successive metal and ceramic layers. Two competing modes were observed and modeled: (i) fracture by coplanar crack growth within successive ceramic layers ahead of the initial crack, and (ii) multiple cracking within the ceramic layers. It was found that plastic yielding of the metal layers encourages single, coplanar crack growth instead of multiple cracking. This result is surprising because the single crack pattern is the low-energy mode, and the multiple crack pattern is the high-energy mode.

In this paper, we analyze a simple, idealized problem. We consider a body with an elastic phase adjoining two strips of material that can deform plastically (see Figure 1). It is assumed that a crack exists in the elastic phase, oriented perpendicular to the interface. Plane strain conditions are assumed and the body is subject to tensile loading. The elastic properties are taken to be uniform throughout the body. Attention is focussed on the issue of whether the crack will penetrate the interface or be deflected into it and the subsequent crack propagation process. Full finite strain transient analyses are carried out. The constitutive relation for the block material is that of an isotropic hardening elastic-viscoplastic solid. Two characterizations of the material strain rate sensitivity are considered. In some calculations, a pure power law relation is used, while in others the enhanced strain rate sensitivity exhibited by many metals at high strain rates, e.g., Campbell and Ferguson, (1970), Klopp et al. (1985), is modeled.

The analyses are carried out using a cohesive surface framework, where the fracture characteristics of the material are embedded in the cohesive surface traction-displacement separation relation, Needleman, (1987), Xu and Needleman, (1994). Crack initiation, crack growth and crack arrest emerge naturally as outcomes of the imposed loading and are calculated directly in terms of the properties of the material and of the parameters characterizing the cohesive surface separation law. The cohesive parameters include a strength and the work of separation per unit area so that, from dimensional considerations, a characteristic length enters the formulation. This cohesive surface framework has been used previously to model quasi-static crack growth in plastically deforming solids, e.g., Needleman, (1990a, b), Tvergaard and Hutchinson, (1992, 1996), dynamic crack growth, e.g., Xu and Needleman, (1994) and Siegmund and Needleman, (1997), and reinforcement cracking in metal matrix composites, Finot et al. (1994). It is of interest to note that Finot et al. (1994) found in their quasi-static

analysis that stable equilibrium solutions did not exist for certain parameter values; i.e., crack growth would take place dynamically.

The material and cohesive parameters are chosen to give deformation behavior and toughness values representative of a structural steel. Thus, the situation modeled can be regarded as pertaining to the propagation of a crack originating in an iron-carbide particle into the surrounding ferrite.

2. Formulation

The cohesive surface formulation and numerical method follow those in Xu and Needleman, (1994) and Siegmund and Needleman, (1997). A finite strain Lagrangian formulation is used, with the initial undeformed configuration taken as reference, so that all field quantities are considered to be functions of convected coordinates, y^i, which serve as particle labels, and time t. The principle of virtual work is written as

$$\int_V \mathbf{s}\colon \delta\mathbf{F}\,\mathrm{d}V - \int_{S_{\text{int}}} \mathbf{T}\cdot\delta\boldsymbol{\Delta}\,\mathrm{d}S = \int_{S_{\text{ext}}} \mathbf{T}\cdot\delta\mathbf{u}\,\mathrm{d}S - \int_V \rho\frac{\partial^2\mathbf{u}}{\partial t^2}\cdot\delta\mathbf{u}\,\mathrm{d}V \tag{1}$$

where $\mathbf{s}$ is the nonsymmetric nominal stress tensor, $\mathbf{u}$ is the displacement vector, $\mathbf{F}$ is the deformation gradient, $\boldsymbol{\Delta}$ is the displacement jump across the cohesive surface, $\mathbf{A} : \mathbf{B}$ denotes $A^{ij}B_{ji}$, and V, S_{ext} and S_{int} are the volume, external surface area and internal cohesive surface area, respectively, of the body in the reference configuration. The density of the material in the reference configuration is ρ and the traction vector $\mathbf{T}$ and the reference configuration normal $\mathbf{n}$ are related by $\mathbf{T} = \mathbf{n}\cdot\mathbf{s}$. Also, $\mathbf{s} = \mathbf{F}^{-1}\cdot\boldsymbol{\tau}$, where $\boldsymbol{\tau}$ is the Kirchhoff stress, $\boldsymbol{\tau} = \det(\mathbf{F})\boldsymbol{\sigma}$, with $\boldsymbol{\sigma}$ being the Cauchy stress.

Computations are carried out for center cracked bimaterial specimens, with the interface being perpendicular to the plane of the initial crack, as sketched in Figure 1. In the reference configuration, the specimen has height $2L$, width $2w$ and a crack of length $2a_i$ along $y^2 = 0$ (see Figure 1). Plane strain conditions are assumed to prevail and a Cartesian coordinate system is used as reference, with the $y^1 - y^2$ plane as the plane of deformation. Symmetry about $y^1 = 0$ is presumed so that only one half of the specimen is analyzed numerically.

The initial crack is specified by

$$T^1 = 0, \qquad T^2 = 0 \quad \text{on } y^2 = 0 \text{ and } -a_i \leqslant y^1 \leqslant a_i. \tag{2}$$

At $t = 0$, the body is stress free and at rest. Equal and opposite normal velocities are prescribed on the edges at $y^2 = \pm L$, with the shear traction taken to vanish there. The edges at $y^1 = \pm w$ are traction free so that the boundary conditions on the region analyzed numerically are

$$u_1 = 0, \qquad T^2 = 0 \quad \text{on } y^1 = 0, \tag{3}$$

$$T^1 = 0, \qquad T^2 = 0 \quad \text{on } y^1 = w, \tag{4}$$

$$u_2 = \pm\int V(t)\,\mathrm{d}t, \qquad T^1 = 0 \quad \text{on } y^2 = \pm L, \tag{5}$$

where in (5)

$$V(t) = \begin{cases} V_1 t/t_r, & \text{for } t \leqslant t_r; \\ V_1, & \text{for } t > t_r. \end{cases} \tag{6}$$

Symmetry of the solution about $y^2 = 0$ is expected due to the symmetry of the geometry and loading. However, asymmetry can develop because of numerical instabilities.

The constitutive relation is that of an elastic–viscoplastic isotropic hardening solid, with any effects of the temperature rise accompanying plastic dissipation neglected. The total rate of deformation, $\mathbf{D} = \text{sym}(\dot{\mathbf{F}} \cdot \mathbf{F}^{-1})$, is written as the sum of an elastic part, $\mathbf{D}^e$, and a plastic part, $\mathbf{D}^p$, so that

$$\mathbf{D} = \mathbf{D}^e + \mathbf{D}^p. \tag{7}$$

Small elastic strains and elastic isotropy are presumed so that

$$\mathbf{D}^e = \mathcal{L}^{-1} : \hat{\boldsymbol{\tau}}, \tag{8}$$

with $\hat{\boldsymbol{\tau}}$ the Jaumann rate of Kirchhoff stress and

$$\mathcal{L} = \frac{E}{1+\nu}\left[\mathbf{I}' + \frac{\nu}{1-2\nu}\mathbf{I} \otimes \mathbf{I}\right], \tag{9}$$

where E is Young's modulus, ν is Poisson's ratio, $\mathbf{I}$ and $\mathbf{I}'$ are the second and fourth order identity tensors, respectively, and $\otimes$ denotes the tensor product, $(\mathbf{A} \otimes \mathbf{B})^{ijkl} = A^{ij}B^{kl}$.

The viscoplastic flow law is

$$\mathbf{D}^p = \frac{3\dot{\bar{\varepsilon}}}{2\bar{\sigma}}\boldsymbol{\tau}' \tag{10}$$

where the effective plastic strain rate $\dot{\bar{\varepsilon}}$ is

$$\dot{\bar{\varepsilon}} = \sqrt{\tfrac{2}{3}\mathbf{D}^p : \mathbf{D}^p} \tag{11}$$

and

$$\boldsymbol{\tau}' = \boldsymbol{\tau} - \tfrac{1}{3}(\boldsymbol{\tau} : \mathbf{I})\mathbf{I}, \qquad \bar{\sigma}^2 = \tfrac{3}{2}\boldsymbol{\tau}' : \boldsymbol{\tau}', \tag{12}$$

$$\dot{\bar{\varepsilon}} = R(\bar{\sigma}/g(\bar{\varepsilon})), \qquad g(\bar{\varepsilon}) = \sigma_0(\bar{\varepsilon}/\varepsilon_0 + 1)^N, \qquad \varepsilon_0 = \sigma_0/E. \tag{13}$$

Here, a superposed dot denotes differentiation with respect to time, $\bar{\varepsilon} = \int \dot{\bar{\varepsilon}}\, dt$, σ_0 is a reference flow strength, N is the strain hardening exponent and $R(\,)$ is a strain rate hardening function.

In some computations R is taken to be a pure power law, i.e.,

$$R(x) = \dot{\varepsilon}_1(x) = \dot{\varepsilon}_0 x^{1/m}, \tag{14}$$

where $\dot{\varepsilon}_0$ is a reference strain rate and m is the strain rate hardening exponent. In other calculations, the increased rate sensitivity at high strain rates is accounted for. Then, as in Zhou et al. (1994)

$$R(x) = \frac{\dot{\varepsilon}_1(x)\dot{\varepsilon}_2(x)}{\dot{\varepsilon}_1(x) + \dot{\varepsilon}_2(x)}, \tag{15}$$

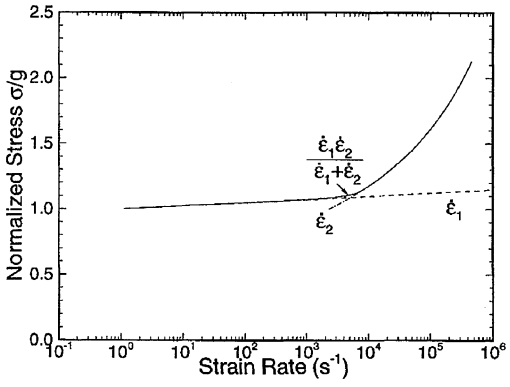

Figure 2. Dependence of the normalized flow strength, $\overline{\sigma}/g$, on plastic strain rate, $\dot{\bar{\varepsilon}}$.

with $\dot{\varepsilon}_1(x)$ given by (14) and

$$\dot{\varepsilon}_2(x) = \dot{\varepsilon}_m \exp\left[-\frac{a}{x}\right]. \tag{16}$$

The form (15) provides a smooth transition between a power law at low strain rates, (14), and an exponential relation at high strain rates, (15), as shown in Figure 2. The exponential relation gives rise to an enhanced strain rate sensitivity at high strain rates, as found experimentally, for example, by Campbell and Ferguson, (1970) and by Klopp et al. (1985). Materials characterized by (14) will be referred to as power law strain rate hardening materials, with results in figures labeled by $\dot{\varepsilon}_1$. Materials characterized by (15) will be referred to as materials with enhanced strain rate hardening, with results in figures labeled by $\dot{\varepsilon}_1\dot{\varepsilon}_2/(\dot{\varepsilon}_1 + \dot{\varepsilon}_2)$.

The constitutive law for the cohesive surfaces is taken to be elastic so that any dissipation associated with separation is neglected. The traction across a cohesive surface is given by

$$\mathbf{T} = -\frac{\partial \phi}{\partial \boldsymbol{\Delta}}. \tag{17}$$

The specific form of the potential ϕ used in this investigation is that given in Xu and Needleman, (1993), which allows for tangential, as well as normal, decohesion

$$\begin{aligned}\phi(\boldsymbol{\Delta}) = \phi_n + \phi_n \exp\left(-\frac{\Delta_n}{\delta_n}\right)\left\{\left[1 - r + \frac{\Delta_n}{\delta_n}\right]\frac{1-q}{r-1}\right. \\ \left. - \left[q + \left(\frac{r-q}{r-1}\right)\frac{\Delta_n}{\delta_n}\right]\exp\left(-\frac{\Delta_t^2}{\delta_t^2}\right)\right\}\end{aligned} \tag{18}$$

where $\Delta_n = \mathbf{n} \cdot \boldsymbol{\Delta}$ and $\Delta_t = \mathbf{t} \cdot \boldsymbol{\Delta}$, with $\mathbf{n}$ and $\mathbf{t}$ as the normal and tangent, respectively, to the surface at a given point in the reference configuration. Also, $q = \phi_t/\phi_n$ and $r = \Delta_n^*/\delta_n$, where Δ_n^* is the value of Δ_n after complete shear separation with normal traction $T_n = 0$. The normal work of separation, ϕ_n, and the shear work of separation, ϕ_t, can be written as

$$\phi_n = e\sigma_{\max}\delta_n \qquad \phi_t = \sqrt{\frac{e}{2}}\tau_{\max}\delta_t. \tag{19}$$

Here, $e = \exp(1)$, $\sigma_{\max}$ and $\tau_{\max}$ are the cohesive surface normal strength and tangential strength, respectively, and δ_n and δ_t are corresponding characteristic lengths.

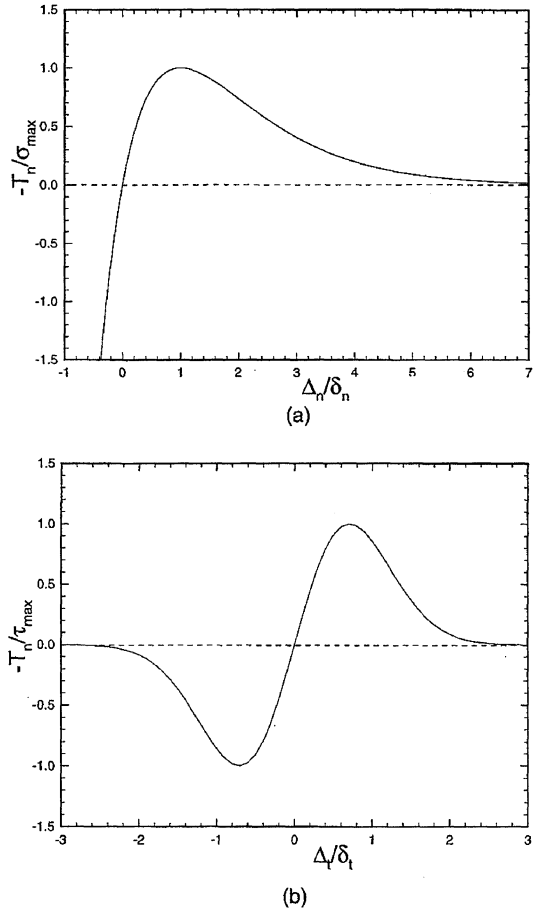

Figure 3. (a) Normalized normal traction, $T_n/\sigma_{\max}$, across the cohesive surface as a function of Δ_n/δ_n with $\Delta_t = 0$. (b) Normalized shear traction, $T_t/\tau_{\max}$, across the cohesive surface as a function of Δ_t/δ_t with $\Delta_n = 0$.

The normal traction across the surface, T_n, as a function of Δ_n with $\Delta_t \equiv 0$ is shown in Figure 3(a). The maximum value of $-T_n$ is $\sigma_{\max}$ and occurs when $\Delta_n = \delta_n$. The variation of shear traction T_t with Δ_t when $\Delta_n \equiv 0$ is shown in Figure 3(b). The maximum value of $|T_t| = \tau_{\max}$ is attained when $|\Delta_t| = \sqrt{2}\delta_t/2$.

The finite element discretization is based on linear displacement triangular elements that are arranged in a 'crossed-triangle' quadrilateral pattern. The equations that result from substituting the finite element discretization into (1) are of the form

$$\mathbf{M}\frac{\partial^2 \mathbf{U}}{\partial t^2} = \mathbf{R}, \tag{20}$$

where $\mathbf{M}$ is a mass matrix, $\mathbf{U}$ is the nodal displacement vector and $\mathbf{R}$ is the nodal force vector. The equations of motion (20) are integrated numerically by an explicit integration procedure, the Newmark β-method with $\beta = 0$, Belytschko et al. (1976). A lumped mass matrix is used instead of the consistent mass matrix, since this has been found preferable for explicit time integration procedures, from the point of view of accuracy as well as computational efficiency, Krieg and Key, (1973). The constitutive updating is based on the rate tangent modulus method of Peirce et al. (1984).

3. Numerical results

Calculations are carried out for specimens having $L = 15\,\text{mm}$, $w = 30\,\text{mm}$, $x_{\text{int}} = 11.2\,\text{mm}$, and $a_i = 10\,\text{mm}$ in Figure 1. Attention is confined to circumstances where the elastic and cohesive properties are uniform throughout the specimen; the plastic flow properties differ across the interface and the cohesive properties of the interface differ from those in the bulk of the specimen. The material in the central region of the specimen is taken to be elastic, $\mathbf{D}^p \equiv 0$ in (7), while the material in the regions on either side is elastic–viscoplastic (see Figure 1). The elastic properties and density are taken to be representative of a steel with $E = 211\,\text{GPa}$, $\nu = 0.3$ and $\rho = 7800\,\text{kg/m}^3 = 7.8 \times 10^{-3}\,\text{MPa/(m/s)}^2$. The dilatational, shear and Rayleigh wave speeds are 6034 m/s, 3226 m/s and 2987 m/s, respectively.

Two values of the flow strength parameter, σ_0, are considered; $\sigma_0 = 1000\,\text{MPa}$ and $\sigma_0 = 600\,\text{MPa}$. The remaining plastic flow parameters are $N = 0.1$, $m = 0.01$, $\dot{\varepsilon}_0 = 1/\text{s}$, $\dot{\varepsilon}_m = 5 \times 10^7/\text{s}$, $a = 10$. With this choice of parameter values the transition from power law strain rate hardening to enhanced strain rate hardening takes place at a strain rate of about $5 \times 10^3/\text{s}$ (see Figure 2). With $\sigma_0 = 1000\,\text{MPa}$, the material parameters are identical to one case in Siegmund and Needleman, (1997). The case $\sigma_0 = 600\,\text{MPa}$ is considered to illustrate low flow strength response.

The imposed velocity $V_1 = 2.5\,\text{m/s}$ and the rise time $t_r = 0.1\,\mu\text{s}$ are fixed for all calculations. Assuming linear elastic response, an imposed velocity of 2.5 m/s corresponds to a stress of 117 MPa carried by the loading wave. The time for the loading wave to travel from a loaded edge of the specimen to the initial crack line is $2.49\,\mu\text{s}$.

The cohesive surface characteristic lengths are fixed at $\delta_n = \delta_t = 0.4\,\mu\text{m}$ for the cohesive surfaces in the bulk phases as well as for the interface cohesive surface. The strength parameters for the cohesive surfaces in the bulk phases are taken as $\sigma_{\max} = 3000\,\text{MPa}$ and $\tau_{\max} = 6990\,\text{MPa}$, which gives $\phi_n = \phi_t = \phi^{\text{bulk}} = 3.26\,\text{KJ/m}^2$. With $\sigma_{\max} = 3000\,\text{MPa}$, $\sigma_0 = 1000\,\text{MPa}$ and $\sigma_0 = 600\,\text{MPa}$ correspond to $\sigma_{\max}/\sigma_0 = 3$ and $\sigma_{\max}/\sigma_0 = 5$. Subsequently, these are referred to as the high flow strength case and the low flow strength case, respectively. For comparison purposes some calculations are carried out where the response on both sides of the interface is elastic. In the following, this case is denoted by $\sigma_{\max}/\sigma_0 = 0$. The remaining cohesive surface parameter, $r = \Delta_n^*/\delta_n$, is taken to have the fixed value $r = 0.0$.

The cohesive surface property values are phenomenological parameters describing the material toughness. The values in Siegmund and Needleman, (1997), where attention was restricted to normal separation, were found to predict representative fracture behavior. Here, the cohesive surface parameters are the same as those in Siegmund and Needleman, (1997), except for the values of the cohesive surface characteristic lengths. The values $\delta_n = \delta_t = 0.4\,\mu\text{m}$ are smaller than in Siegmund and Needleman, (1997), giving rise to a smaller value of the work of separation, ϕ^{bulk}, and hence to a somewhat more brittle fracture behavior. There is no direct basis for assigning values to the cohesive surface tangential properties. We take the tangential work of separation, ϕ_t, and the tangential characteristic length, δ_t, to have the same values as for normal separation. This implies, from (19), that $\tau_{\max} > \sigma_{\max}$. In the results to be presented subsequently crack growth in the bulk materials is essentially mode I, so that the tangential cohesive properties do not play a significant role in the bulk response (as long as they are such as to preclude deviation from the straight ahead crack path).

Two sets of values of the interface strength parameters $\sigma_{\max}^{\text{int}}$ and $\tau_{\max}^{\text{int}}$ are considered. In both cases, the ratio of $\sigma_{\max}^{\text{int}}$ to $\tau_{\max}^{\text{int}}$ is taken to be such that $\phi_n^{\text{int}} = \phi_t^{\text{int}} = \phi^{\text{int}}$. The two sets of values are $\sigma_{\max}^{\text{int}} = 450\,\text{MPa}$ and $\tau_{\max}^{\text{int}} = 1048\,\text{MPa}$, which gives $\phi^{\text{int}} = 0.489\,\text{KJ/m}^2$,

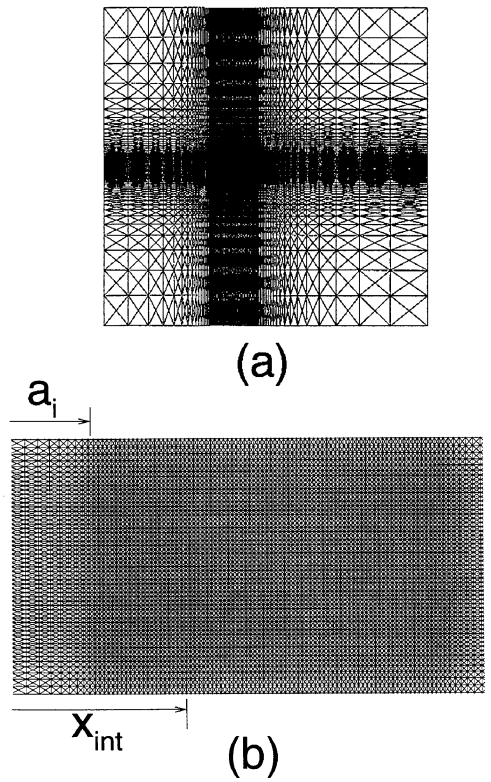

Figure 4. (a) A 125 × 90 element finite element mesh. (b) The mesh near the initial crack tip of (a).

and $\sigma_{\max}^{\text{int}} = 750\,\text{MPa}$ and $\tau_{\max}^{\text{int}} = 1750$, which gives $\phi^{\text{int}} = 0.815\,\text{KJ/m}^2$. In the former case, $\phi^{\text{int}} = 0.15\phi^{\text{bulk}}$, while in the latter case $\phi^{\text{int}} = 0.25\phi^{\text{bulk}}$. The quasi-static crack deflection analysis of He and Hutchinson, (1989) suggests that the change from crack penetration to symmetric crack deflection into an interface occurs when the ratio of the energy release rate for straight ahead crack growth is about 0.2 times the energy release rate for crack deflection into the interface. The two sets of interface strength values were chosen to straddle this transition.

The finite element mesh consists of 11,250 quadrilateral elements, Figure 4(a), with a uniform region ahead of the initial crack surrounded by a graduated mesh out to the specimen boundaries. The cohesive surfaces are all the lines in the plane of deformation defined by the element boundaries. The uniform region has 80 × 40 square elements, with side length 0.05 mm, as shown in Figure 4(b). The uniform mesh region extends 4 mm in front of the initial crack tip and 1 mm above and below the initial crack line. The calculations are terminated when the current crack tip is near the end of the uniform mesh region. The ratio of the mesh spacing in the uniform region to cohesive surface characteristic length is 125. By way of comparison, the fine mesh used in Xu and Needleman, (1994) had a ratio of the mesh spacing in the uniform region to cohesive surface characteristic length of 6.25. Xu and Needleman, (1994) also carried out computations with a coarser mesh for which the ratio of the mesh spacing in the uniform region to cohesive surface characteristic length was ≈ 47 and found a delay in dynamic crack branching as compared with the finer mesh. Thus, crack branching in the elastic phase cannot be represented accurately with the mesh used. Nevertheless, as will be shown subsequently, the present mesh can resolve the main features of crack growth of interest in this study.

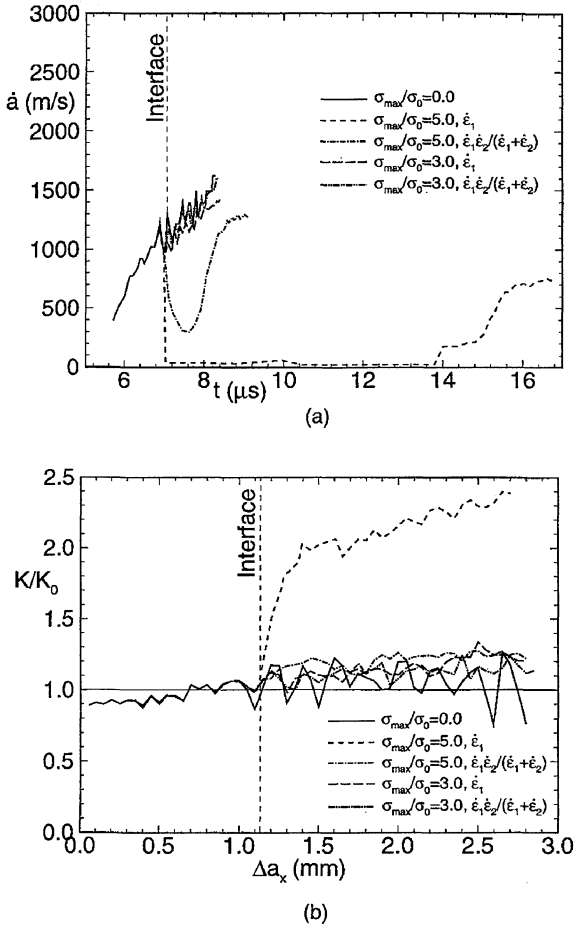

Figure 5. The crack growth behavior for a two phase material with a strong interface ($\sigma_{\max}^{\text{int}} = 750\,\text{MPa}$, $\sigma_{\max} = 3000\,\text{MPa}$, $\tau_{\max}^{\text{int}} = 1750\,\text{MPa}$, $\tau_{\max} = 6990\,\text{MPa}$) and various ratios $\sigma_{\max}/\sigma_0$, for both power law strain rate hardening and enhanced strain rate hardening. The impact velocity is $V_1 = 2.5\,\text{m/s}$. (a) Crack speed, $\dot{a}$, versus time, t. (b) Normalized stress intensity factor, K/K_0, versus crack growth, Δa_x.

Figures 5 to 9 show results for $\phi^{\text{int}} = 0.25\phi^{\text{bulk}}$. In all cases in Figures 5 to 9, the crack path is not deflected by the interface and crack growth takes place along the initial crack line.

The effect of varying the flow strength, σ_0, and the characterization of the strain rate hardening on the crack speed, $\dot{a}$, versus time response is shown in Figure 5(a). The crack speed is computed from crack extension versus time data, where the crack location is identified with $\Delta_n \geqslant 5\delta_n$, by successive three point least squares linear fits; i.e. through points 1 to 3, points 2 to 4, etc[1]. For an elastic solid, $\sigma_{\max}/\sigma_0 = 0$, the crack speed begins to oscillate when $\dot{a}$ is about 40 percent of the Rayleigh wave speed, which is attained just prior to the crack reaching the interface. The crack speed continues to oscillate and increases to about 50 percent of the elastic wave speed. Attempted crack branching is first seen after the crack has crossed the interface, but, most likely, is not successful because of the rather large ratio of mesh spacing to cohesive surface characteristic length. For the other cases in Figure 5(a), where the response of the surrounding phase is viscoplastic, the crack speed history in the elastic phase is essentially the same as for the elastic specimen. However, once the crack has reached the interface, the

[1] This was the procedure used for calculating the crack speed from crack extension versus time values in previous studies and was incorrectly called a 'quadratic polynomial' fit in Xu and Needleman, (1994).

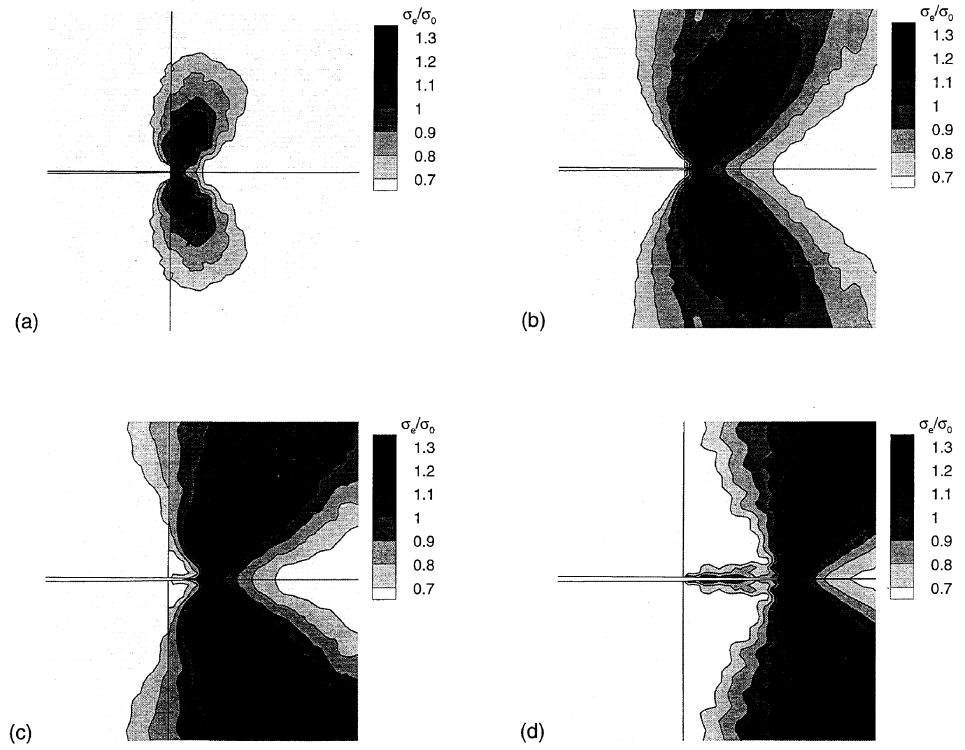

Figure 6. Contours of Mises effective stress, σ_e, with $\sigma_{\max}^{\text{int}} = 750\,\text{MPa}$, $\sigma_{\max} = 3000\,\text{MPa}$, $\tau_{\max}^{\text{int}} = 1750\,\text{MPa}$, $\tau_{\max} = 6990\,\text{MPa}$ and $\sigma_0 = 600\,\text{MPa}$ and power law strain rate hardening. The impact velocity is $V_1 = 2.5\,\text{m/s}$. The extent of the region shown is 3 mm × 3 mm. (a) $t = 7.52\,\mu\text{s}$, $\Delta a_x = 1.2\,\text{mm}$, $\dot{a}_x = 0.0\,\text{m/s}$. (b) $t = 10.0\,\mu\text{s}$, $\Delta a_x = 1.3\,\text{mm}$, $\dot{a}_x = 56\,\text{m/s}$. (c) $t = 14.6\,\mu\text{s}$, $\Delta a_x = 1.55\,\text{mm}$, $\dot{a}_x = 206\,\text{m/s}$. (d) $t = 16.0\,\mu\text{s}$, $\Delta a_x = 2.2\,\text{mm}$, $\dot{a}_x = 706\,\text{m/s}$.

crack growth behavior is strongly influenced by the material parameters in the viscoplastic constitutive description.

For a low flow strength, $\sigma_{\max}/\sigma_0 = 5$, and power-law strain rate hardening the crack is temporarily arrested at the interface. Subsequently, after several wave reflections, the crack reinitiates and moves away from the interface. The crack speed increases to about 750 m/s before the end of the uniform mesh region is reached. With enhanced strain rate hardening (and $\sigma_{\max}/\sigma_0 = 5$), crack arrest does not occur. The crack speed decreases when the crack crosses the interface and then increases to about 1300 m/s, which is greater than the crack speed attained before reaching the interface.

For a high flow strength, $\sigma_{\max}/\sigma_0 = 3$, the presence of the interface and the change in the material properties across it has little effect on the crack growth behavior, both for the power-law and enhanced strain rate hardening cases. In fact, the crack speeds are similar to the elastic case where there is no change of material properties across the interface. This is clearly because little plastic flow occurs for the high strength material. A significant difference between the situation analyzed here and that for a homogeneous material in Siegmund and Needleman, (1997) is that in the present circumstances plastic straining does not take place until after crack propagation has begun.

Figure 5(b) shows curves of the normalized stress intensity factor K/K_0, versus crack growth, Δa_x. Here, Δa_x denotes the amount of crack growth in the direction parallel to the

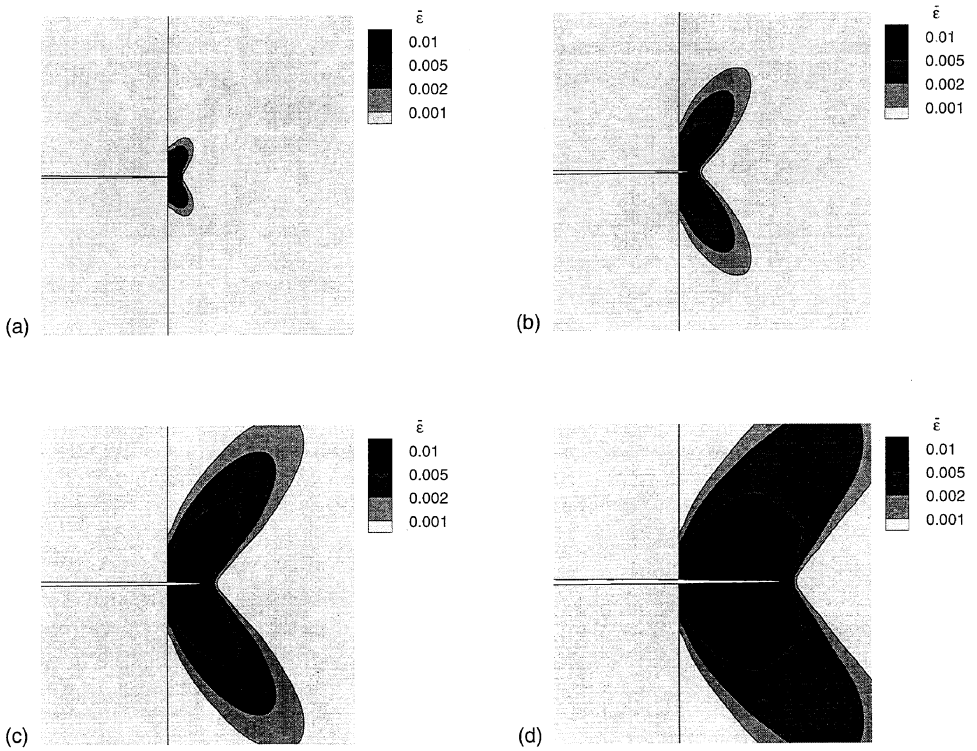

Figure 7. Contours of equivalent plastic strain, $\bar{\varepsilon}$, with $\sigma_{\max}^{\text{int}} = 750$ MPa, $\sigma_{\max} = 3000$ MPa, $\tau_{\max}^{\text{int}} = 1750$ MPa, $\tau_{\max} = 6990$ MPa and $\sigma_0 = 600$ MPa and power law strain rate hardening. The impact velocity is $V_1 = 2.5$ m/s. The extent of the region shown is 3 mm × 3 mm. (a) $t = 7.52\,\mu$s, $\Delta a_x = 1.2$ mm, $\dot{a}_x = 0.0$ m/s. (b) $t = 10.0\,\mu$s, $\Delta a_x = 1.3$ mm, $\dot{a}_x = 56$ m/s. (c) $t = 14.6\,\mu$s, $\Delta a_x = 1.55$ mm, $\dot{a}_x = 206$ m/s. (d) $t = 16.0\,\mu$s, $\Delta a_x = 2.2$ mm, $\dot{a}_x = 706$ m/s.

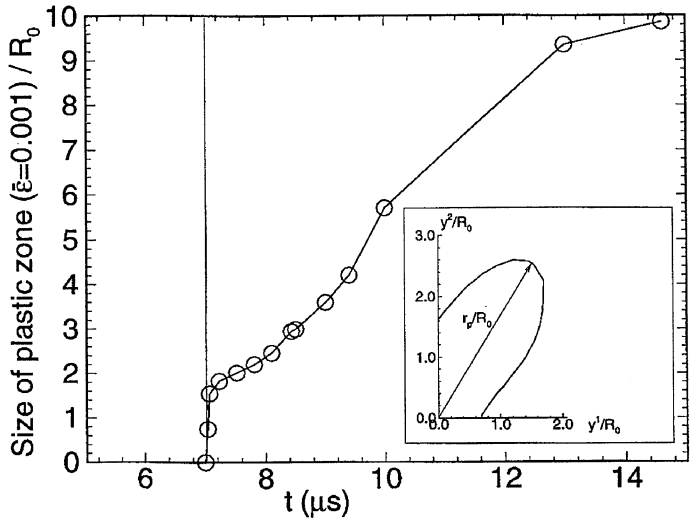

Figure 8. The normalized plastic zone size r_p/R_0 for $\sigma_{\max}/\sigma_0 = 5$ and power-law strain rate hardening. The interface strength is specified by $\sigma_{\max}^{\text{int}} = 750$ MPa and $\tau_{\max}^{\text{int}} = 1750$ MPa. The insert shows how r_p is measured from the contour $\bar{\varepsilon} = 0.001$.

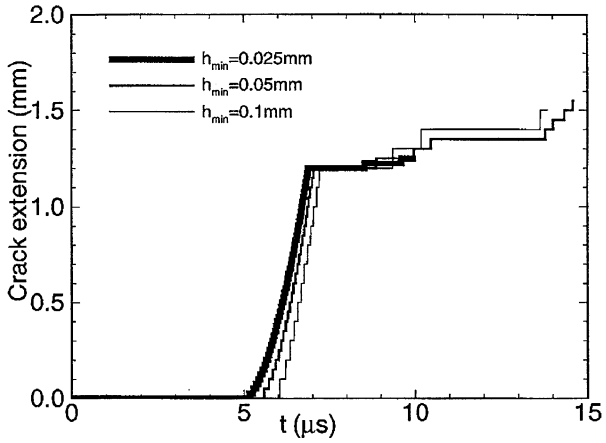

Figure 9. Curves of crack extension versus time for three finite element meshes. $h_{\min}$ is the mesh spacing in the uniform mesh region. The calculations were carried out using $\sigma_{\max}/\sigma_0 = 5$ with power-law strain rate hardening and interface strength values of $\sigma_{\max}^{\text{int}} = 750\,\text{MPa}$ and $\tau_{\max}^{\text{int}} = 1750\,\text{MPa}$.

initial crack line. The stress intensity factor K is computed from the J-integral using the small scale yielding relation

$$K = \sqrt{\frac{EJ}{(1-\nu^2)}}, \tag{21}$$

where, under dynamic loading conditions the value of the J-integral, Rice, (1968), involves an area integral as well as a line integral, Nakamura et al. (1985)

$$J = \int_\Gamma \left[(W+L)n_1 - \mathbf{T}\cdot\frac{\partial \mathbf{u}}{\partial y^1}\right] \mathrm{d}s + \int_A \left[\rho\frac{\partial \mathbf{v}}{\partial t}\cdot\frac{\partial \mathbf{u}}{\partial y^1} - \rho\mathbf{v}\cdot\frac{\partial \mathbf{v}}{\partial y^1}\right] \mathrm{d}A. \tag{22}$$

In (22), $\mathbf{v} = \partial\mathbf{u}/\partial t$, $W = \int \boldsymbol{\tau}\!:\!\mathbf{D}\,\mathrm{d}t$, $L = \rho\mathbf{v}\cdot\mathbf{v}/2$, Γ is a path surrounding the crack tip and n_1 is the component of the normal to Γ in the y^1-direction. The stress intensity factor (21) provides a measure of the effective crack growth resistance, i.e., of the work of creating new free surface along with any accompanying plastic dissipation.

A reference stress intensity factor K_0 is defined by setting J in (21) to the value of the work of separation for the bulk material, ϕ^{bulk}; with the parameter values used here $K_0 = 27.5\,\text{MPa}\sqrt{\text{m}}$.

Crack growth initiates at $K/K_0 \approx 0.9$; for a sharp crack in an elastic solid $K/K_0 = 1$ at initiation is an exact result, Rice, (1968). The deviation from $K/K_0 = 1$ in Figure 5(b) is, at least in part, a consequence of the rather crude mesh (relative to the cohesive characteristic length δ_n) used in the present calculations. For the elastic solid, $\sigma_{\max}/\sigma_0 = 0$, K/K_0 oscillates about unity during crack growth. With $\sigma_{\max}/\sigma_0 = 5$ and power law strain rate hardening there is a significant increase in the normalized stress intensity factor once the crack reaches the interface. The stress intensity factor increases rapidly during the early stages of crack growth after reaching the interface, while the increase is less pronounced during the latter stages of crack growth. For $\sigma_{\max}/\sigma_0 = 5$ and enhanced strain rate hardening – where only a decrease in velocity but no arrest is observed – the increase in K/K_0 is much less pronounced. For the elastic solid as well as for the high strength material with $\sigma_{\max}/\sigma_0 = 3$, both for power-law strain rate hardening and enhanced strain rate hardening, nearly no increase in K/K_0 occurs.

Figures 6 and 7 show the evolution of the Mises effective stress and of the equivalent plastic strain for the calculation with $\sigma_{\max}/\sigma_0 = 5$ and power-law strain rate hardening. Figures 6(a) and 7(a) are at a time when the crack has just arrested at the interface. The plastically deforming region in Figure 7 is cut-off at the interface by the presence of the elastic phase. The crack remains essentially stationary until the time shown in Figures 6(c) and 7(c) (see Figure 5(a)) so that crack tip fields similar to a stationary crack are present in Figures 6(b) and 7(b). The field distributions in Figures 6(d) and 7(d) are those for a growing crack.

The growth of the size of the plastic zone for this case is plotted in Figure 8. The size of the plastic zone is identified with the contour $\bar{\varepsilon} = 0.001$ in the direction of its largest extent as depicted in the insert of Figure 8. The size of the plastic zone is normalized by the reference value $R_0 = (K_0/\sigma_0)^2/(3\pi) \approx 0.22\,\text{mm}$. There is nearly no plastic deformation before the crack reaches the interface. Then, the plastic zone develops very quickly up to the point where $r_p/R_0 \approx 1.5$. During the time interval of crack arrest, $7.25\,\mu\text{s} - 14\,\mu\text{s}$, the size of the plastic zone increases at a rather constant rate. The growth rate, $\dot{r}_p$, in this time interval was determined by a linear fit to the data points shown and was found to be approximately 215 m/s. Fields and deWit, (1990) experimentally found plastic zone growth rates for arrested cracks in a pressure vessel steel between 142 m/s and 230 m/s.

Convergence of the calculations was investigated using three meshes with element sizes in the uniform mesh region of 0.1 mm × 0.1 mm, 0.05 mm × 0.05 mm and 0.025 mm × 0.025 mm. The results of the convergence study, which was carried out using $\sigma_{\max}/\sigma_0 = 5$ and power-law strain rate hardening are shown in Figure 9. The finest mesh is in the uniform region so that $h_{\min}$ in Figure 9 is the uniform mesh spacing. The curves of crack extension versus time are in very good agreement for the two finer meshes. The results presented here were obtained using the intermediate mesh with $h_{\min} = 0.05\,\text{mm}$.

Figures 10 to 15 show crack growth results for the cases with $\phi^{\text{int}} = 0.15\phi^{\text{bulk}}$. In all cases in Figures 10 to 15 the crack grows within the elastic phase in the y^1-direction, but when the crack reaches the interface crack growth in the y^1-direction stops and crack growth then occurs in y^2-direction, i.e., the crack deflects into the interface. In the interface, the location of the crack tip is defined by $\Delta_t \geqslant 5\delta_t$. The amount of crack growth in the interface is denoted by Δa_y, which is the distance between one of the two symmetrically located crack tips and the initial crack line. The crack speed $\dot{a}_y$ is calculated using successive three point linear least squares fits as described previously.

Figure 10(a) shows curves of crack speed, $\dot{a}$, versus time. Although the crack speed decreases fairly abruptly near the interface and arrests briefly, there is little delay between the arrival of the crack tip at the interface and the initiation of interface crack propagation, even for the material parameters that lead to crack arrest at the interface for the case of the strong interface in Figure 5(a). As for the case of straight ahead crack growth, the crack speed in the elastic phase is identical in all cases. The crack speeds for the interface crack are, however, clearly dependent on the parameters describing the viscoplastic material behavior. The lowest crack speed occurs for the low flow strength material $\sigma_{\max}/\sigma_0 = 5$ with power-law strain rate hardening, $\dot{a}_y$ is in the range 300 m/s to 500 m/s; with enhanced strain rate hardening the crack speed is higher, especially in the initial phase of interface crack growth. The high flow strength material $\sigma_{\max}/\sigma_0 = 3$ gives rise to substantially greater crack speeds; $\dot{a}_y \approx 1500\,\text{m/s}$. The crack speed for the elastic solid, $\sigma_{\max}/\sigma_0 = 0$, is approximately two thirds of the Rayleigh wave speed. Thus, when plastic flow is absent or small, the crack speed that the interface crack attains is higher than the crack speed attained by the crack that grows straight through the interface.

The crack speed is plotted as a function of the crack extension $\Delta a_x + \Delta a_y$ in Figure 10(b). The quantity $\Delta a_x + \Delta a_y$ is the amount of crack extension associated with one of the two symmetrical crack branches; plotting results versus the total crack extension $\Delta a_x + 2\Delta a_y$ would only rescale the abscissa values to the right of the interface line in Figures 10(b) and 10(c). For the elastic solid, $\sigma_{\max}/\sigma_0 = 0$, and for the high flow strength material, $\sigma_{\max}/\sigma_0 = 3$, for both strain rate hardening characterizations, the crack speed in the weak interface is greater than it was at any time before reaching the interface. In contrast, for the low flow strength material, $\sigma_{\max}/\sigma_0 = 5$ the crack speed in the interface is less than it was before approaching the interface. This is a consequence of the increased plastic dissipation with the low strength material.

Curves of the normalized stress intensity factor K/K_0 versus the crack extension $\Delta a_x + \Delta a_y$ are shown in Figure 10(c). Crack growth occurs with $K/K_0 \approx 1$ before the interface is reached. Plastic deformation in the elastic-viscoplastic phase occurs mainly for the low flow strength material, $\sigma_{\max}/\sigma_0 = 5$, with power-law strain rate hardening again leading to more plastic deformation, and hence a larger increase in K/K_0 over unity, than enhanced strain rate hardening. For the high flow strength material, $\sigma_{\max}/\sigma_0 = 3$, and for elastic material behavior, $\sigma_{\max}/\sigma_0 = 0$, the normalized stress intensity factor is slightly above $K/K_0 = 1$ during interface crack growth. It is worth noting that $K/K_0 > 1$ even though the reference stress intensity factor of the interface K_0^{int} is low compared to the reference stress intensity factor of the bulk materials; $K_0^{\text{int}}/K_0 = 0.388$. Hence, the relative increase in toughness, taken as the ratio of the effective crack growth resistance to the toughness of the cohesive surface along which crack growth occurs, is always greater for the deflected crack in Figure 10(c) than for the straight ahead crack growth in Figure 5(b). Since this is true for the elastic material, $\sigma_{\max}/\sigma_0 = 0$, it is a consequence of the change in fields associated with the change in crack propagation direction.

Deformed meshes in the vicinity of the crack tip are shown in Figure 11. For straight ahead crack growth, Figure 11(a), the change in crack profile at the interface can be seen. Figure 11(b) clearly shows the offset of horizontal mesh lines across the interface in Figure 11(b), which arises from the tangential cohesive displacement in the interface. A more quantitative picture of the interface displacement distribution is given in Figure 11(c). The 'mixed-mode' character of the distribution is evident.

As for the strong interface, calculations for the weak interface were carried out using meshes with element sizes in the uniform mesh region of 0.1 mm × 0.1 mm, 0.05 mm × 0.05 mm and 0.025 mm × 0.025 mm. These calculations were continued for 0.2 mm of crack extension into the interface. The variation in response with mesh resolution is similar to that in Figure 9, but with some increase in mesh sensitivity. With $h_{\min} = 0.1$ mm crack growth into the interface begins at $t = 7.3\,\mu$s, whereas with $h_{\min} = 0.025$ mm this occurs at $t = 6.9\,\mu$s.

Figure 12 shows contours of the normalized Mises effective stress σ_e/σ_0 as the crack approaches the interface and deflects into the interface for the case with $\sigma_{\max}/\sigma_0 = 5$ and power law strain rate hardening. As the crack grows symmetrically into the weak interface, two regions of stress concentrations are formed. These regions move apart as the crack propagates along the interface. The regions of high stress concentration remain connected as the crack tips move apart. Note that the contours are very nearly symmetric about the crack line $y^2 = 0$.

Contours of various field quantities are shown in Figures 13 to 15 at the same amount of crack growth into the interface, $\Delta a_y = 0.65$ mm, for four sets of plastic flow properties. The contours of normalized Mises effective stress, σ_e/σ_0 at $\Delta a_y = 0.65$ mm are shown in Figure 13. With $\sigma_{\max}/\sigma_0 = 5$, power law strain rate hardening as well as enhanced strain rate

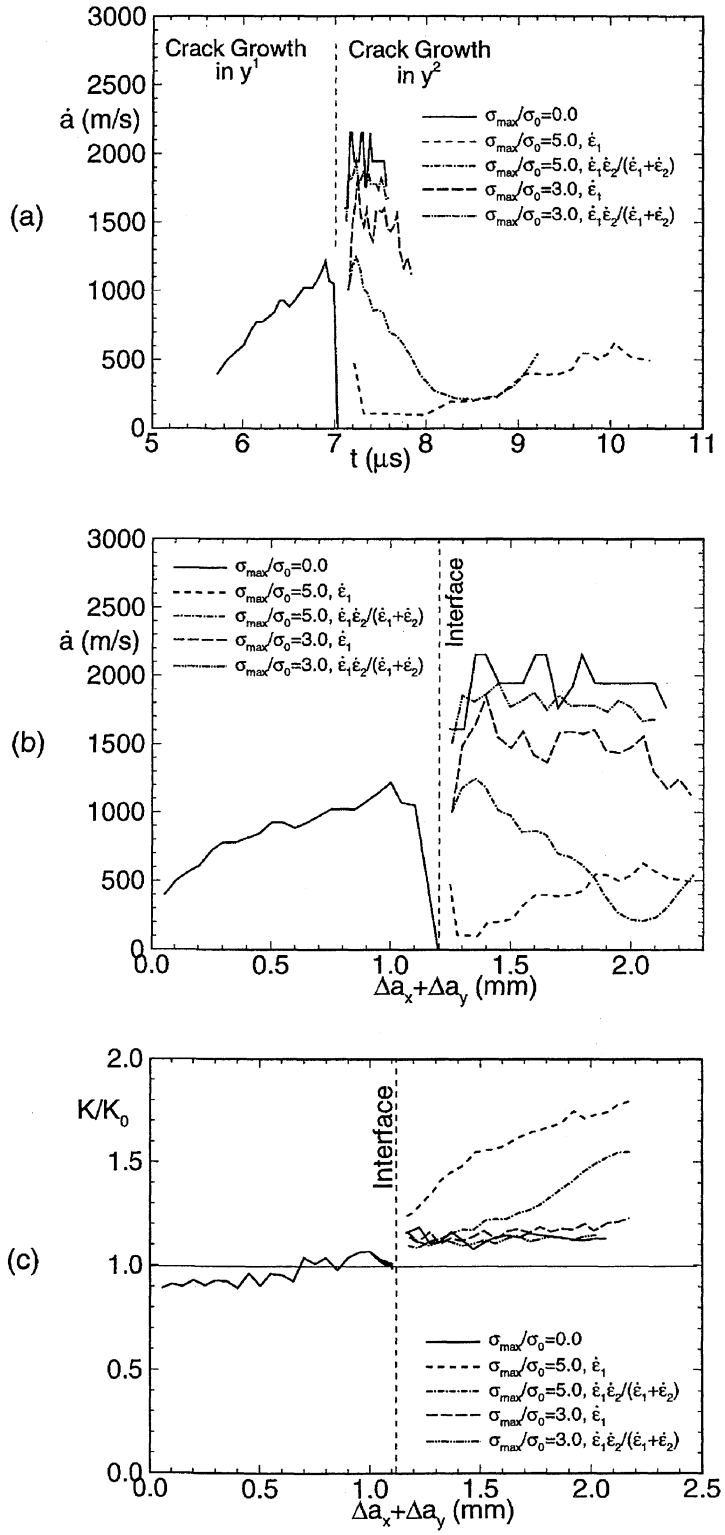

Figure 10. Crack growth behavior for a two phase material with a weak interface ($\sigma_{\max}^{\text{int}} = 450\,\text{MPa}$, $\sigma_{\max} = 3000\,\text{MPa}$, $\tau_{\max}^{\text{int}} = 1048\,\text{MPa}$, $\tau_{\max} = 6990\,\text{MPa}$) and various ratios $\sigma_{\max}/\sigma_0$, for both power law strain rate hardening and enhanced strain rate hardening. The impact velocity is $V_1 = 2.5\,\text{m/s}$. (a) Crack speed, $\dot{a}$, versus time, t. (b) Crack speed, $\dot{a}$, versus crack extension, $\Delta a_x + \Delta a_y$. (c) Normalized stress intensity factor, K/K_0, versus crack extension, $\Delta a_x + \Delta a_y$.

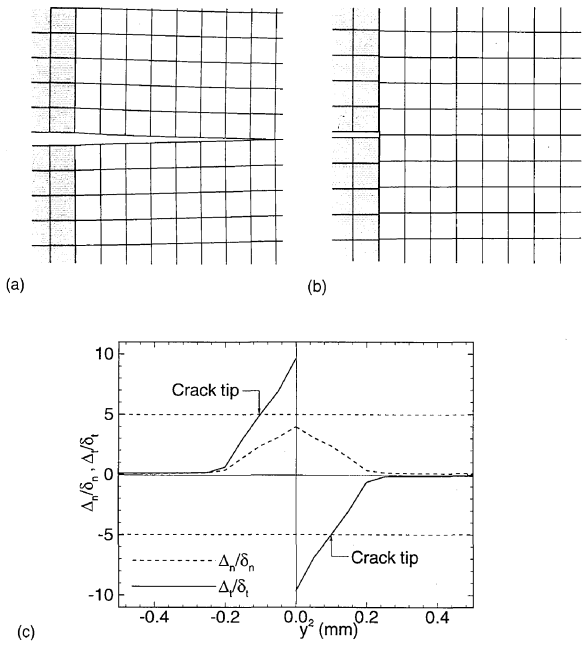

Figure 11. (a) Crack profile for $\sigma_{\max}^{\text{int}} = 750\,\text{MPa}$, $\sigma_{\max} = 3000\,\text{MPa}$, $\tau_{\max}^{\text{int}} = 1750\,\text{MPa}$, $\tau_{\max} = 6990\,\text{MPa}$ at $t = 14.6\,\mu\text{s}$. (b) Crack profile for $\sigma_{\max}^{\text{int}} = 450\,\text{MPa}$, $\sigma_{\max} = 3000\,\text{MPa}$, $\tau_{\max}^{\text{int}} = 1048\,\text{MPa}$, $\tau_{\max} = 6990\,\text{MPa}$ at $t = 8.0\,\mu\text{s}$. (c) Displacement jumps, Δ_n, and Δ_t, as a function of position in the interface for (b). In (a) and (b), the elastic material is shaded and the extent of the region shown is 0.5 mm × 0.5 mm. Power law strain rate hardening and $\sigma_0 = 600\,\text{MPa}$; $V_1 = 2.5\,\text{m/s}$.

hardening gives rise to connected regions of high values of σ_e/σ_0 (Figures 13(a) and 13(b)). On the other hand, for the high flow strength solid, $\sigma_{\max}/\sigma_0 = 3$, for both power law strain rate hardening and for enhanced strain rate hardening (Figures 13(c) and 13(d)), there are two separated regions of high values of σ_e/σ_0.

In all four cases plastic deformation is confined to a layer that extends parallel to the interface up to the crack tip location as seen in Figure 14. The width of this layer decreases with increasing flow strength of the elastic–viscoplastic material. Enhanced strain rate hardening results in a smaller width of the plastic zone than does power-law strain rate hardening. In each plot, the greatest amount of plastic deformation is at the location where the initial crack impinges on the interface. Except for the case with $\sigma_{\max}/\sigma_0 = 5$ and power law strain rate hardening, the width of the plastic zone becomes smaller as the crack propagates along the interface. An increase in plastic deformation as the crack propagates is associated with a decrease in crack speed as also seen for homogeneous materials in Siegmund and Needleman, (1997).

Figures 13(a) and 14(a), where $\Delta a_x + \Delta a_y = 1.85\,\text{mm}$, correspond to a similar stage of crack growth with the same material parameters as in Figures 6(c) and 7(c), where $\Delta a_x = 1.55\,\text{mm}$. The regions of large plastic strain and of high effective stress are larger for the straight ahead crack growth shown in Figures 6(c) and 7(c). If the comparison were made by comparing similar values of total crack advance $\Delta a_x + 2\Delta a_y = 2.5\,\text{mm}$ in Figures 13(a) and 14(a) with $\Delta a_x = 2.2\,\text{mm}$ in Figures 6(d) and 7(d) the discrepancy is even greater.

Contours of the physical stress component σ_{22} (defined by $\sigma_{22} = \tau^{ij} F_{i2} F_{j2}$) are shown in Figure 15 for the four material property combinations considered. For the low flow strength

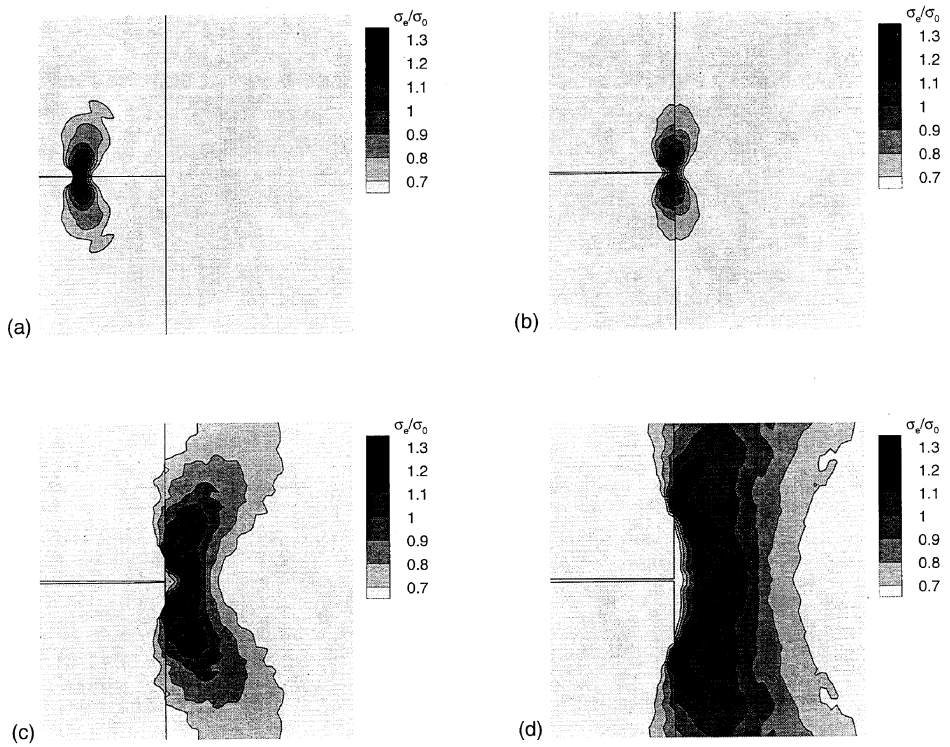

Figure 12. Contours of Mises effective stress, σ_e, with $\sigma_{\max}^{\text{int}} = 450$ MPa, $\sigma_{\max} = 3000$ MPa, $\tau_{\max}^{\text{int}} = 1048$ MPa, $\tau_{\max} = 6990$ MPa and $\sigma_0 = 600$ MPa and power law strain rate hardening. The impact velocity is $V_1 = 2.5$ m/s. The extent of the region shown is 3 mm × 3 mm. (a) $t = 6.16\,\mu$s, $\Delta a_x = 0.35$ mm, $\Delta a_y = 0.0$ mm, $\dot{a}_x = 778$ m/s, $\dot{a}_y = 0$ m/s. (b) $t = 7.0\,\mu$s, $\Delta a_x = 1.2$ mm, $\Delta a_y = 0.0$ mm, $\dot{a}_x = 0$ m/s, $\dot{a}_y = 0$ m/s. (c) $t = 8.0\,\mu$s, $\Delta a_x = 1.2$ mm, $\Delta a_y = 0.20$ mm, $\dot{a}_x = 0$ m/s, $\dot{a}_y = 103$ m/s. (d) $t = 9.62\,\mu$s, $\Delta a_x = 1.2$ mm, $\Delta a_y = 0.65$ mm, $\dot{a}_x = 0$ m/s, $\dot{a}_y = 473$ m/s.

material with power-law strain rate hardening, Figure 15(a) there is a relatively wide zone of medium values of σ_{22}, but a lower peak value of σ_{22} than for the other cases. For the high flow strength material, the peak values of σ_{22} are higher (1167 MPa in Figure 15(c) as compared with 902 MPa in Figure 15(a)); enhanced strain rate hardening leads to a higher peak stress, but a reduced size of the region of concentrated stress (compare Figures 15(a) and 15(b) or Figures 15(c) and 15(d)). In all four cases, the highest values of σ_{22} on the initial crack line occur at some distance from the interface that depends on the viscoplastic material characterization. For example, in Figure 15(a) the maximum value of σ_{22} on the initial crack line is 890 MPa at $y^1 = 11.69$ mm (the interface is at $y^1 = 11.2$ mm), while in Figure 15(d) the corresponding values are 849 MPa and $y^1 = 11.30$ mm.

4. Discussion

Dynamic crack growth across or into an interface has been analyzed using a framework where the crack growth history is a direct outcome of the analysis, determined by the cohesive surface properties (the strength and the work of separation), by the material properties and by the imposed loading. The material on one side of the interface is taken to be elastic, while that on the other side of the interface is elastic-viscoplastic. Attention has been restricted to circumstances where the elastic properties are uniform throughout the specimen.

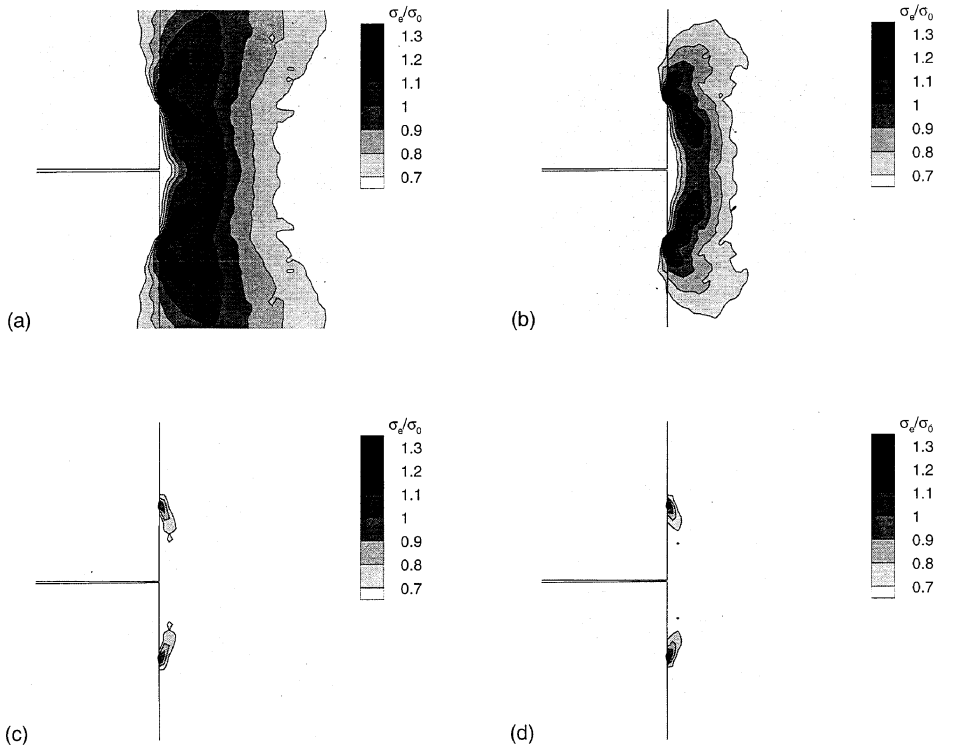

Figure 13. Contours of normalized Mises effective stress, σ_e/σ_0, at $\Delta a_x = 1.2\,\text{mm}$, $\Delta a_y = 0.65\,\text{mm}$ with $\sigma^{\text{int}}_{\max} = 450\,\text{MPa}$, $\sigma_{\max} = 3000\,\text{MPa}$, $\tau^{\text{int}}_{\max} = 1048\,\text{MPa}$, $\tau_{\max} = 6990\,\text{MPa}$. The impact velocity is $V_1 = 2.5\,\text{m/s}$. The extent of the region shown is 3.0 mm × 3.0 mm. (a) Power law strain rate hardening and $\sigma_0 = 600\,\text{MPa}$ ($t = 9.62\,\mu\text{s}$, $\dot{a}_y = 541\,\text{m/s}$). (b) Enhanced strain rate hardening and $\sigma_0 = 600\,\text{MPa}$ ($t = 7.7\,\mu\text{s}$, $\dot{a}_y = 517\,\text{m/s}$). (c) Power law strain rate hardening and $\sigma_0 = 1000\,\text{MPa}$ ($t = 7.5\,\mu\text{s}$, $\dot{a}_y = 1598\,\text{m/s}$). (d) Enhanced strain rate hardening and $\sigma_0 = 1000\,\text{MPa}$ ($t = 7.4\,\mu\text{s}$, $\dot{a}_y = 1777\,\text{m/s}$).

In the cases considered plastic flow is rather limited prior to the crack penetrating the interface or growing along it, which is in contrast to the situations analyzed in Sugimura et al. (1995), where considerable plastic flow occurs before the crack reaches the interface. In the circumstances here, the quasi-static, elastic analysis of He and Hutchinson, (1989) gives an accurate prediction of whether the crack will penetrate the interface or deflect into it. For a low flow strength material with power law strain hardening, and with the interface strength 25 percent of the material cohesive strength, the crack arrests at the interface, but eventually propagates through (Figure 5(a)). This suggests the possibility that with an even lower flow strength, the crack might be permanently arrested at the interface. The comparison between the power law and enhanced strain rate hardening materials in Figure 5(a) then suggests that there may be circumstances where the crack speed in the elastic material plays a determining role in whether or not the crack penetrates the interface – a fast crack would slow down at the interface but penetrate it, while a slower crack would be arrested. For such a composite or layered material, the impact toughness would be much lower than the quasi-static toughness.

Since the results for power law strain hardening can be regarded as having been obtained for circumstances where the transition strain rate is greater than the strain rates occurring anywhere in the material, the comparison between the materials with power law strain rate hardening and enhanced strain rate hardening illustrates cases where strain rates are below and above the transition strain rate, respectively. Thus, whether or not crack arrest occurs at

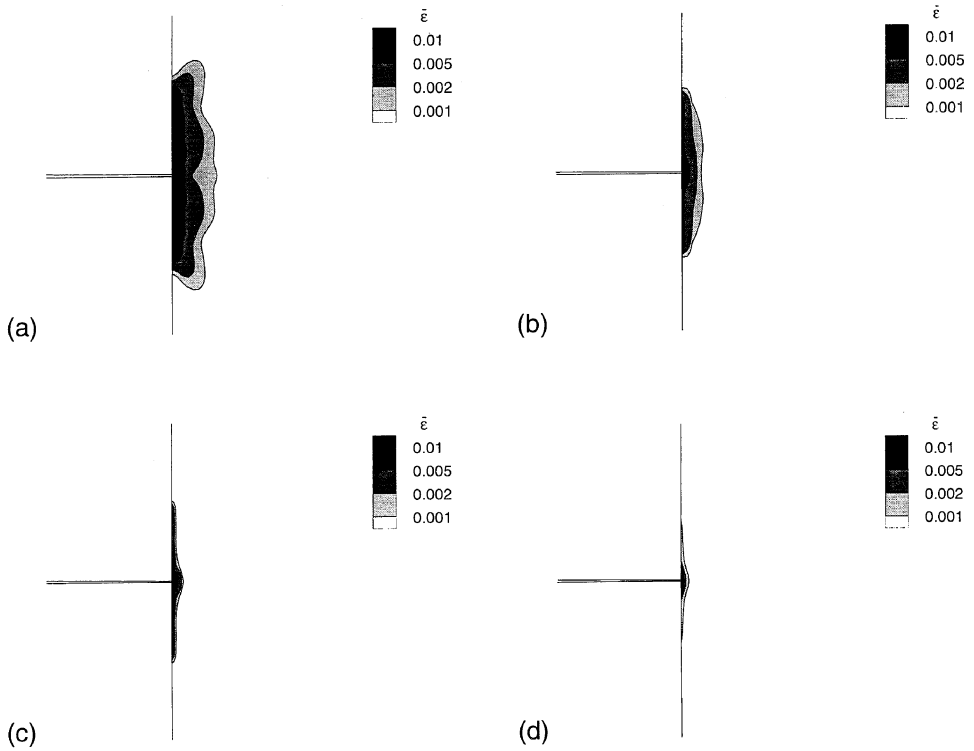

Figure 14. Contours of equivalent plastic strain $\bar{\varepsilon}$ at $\Delta a_x = 1.2\,\text{mm}$, $\Delta a_y = 0.65\,\text{mm}$ with $\sigma_{\max}^{\text{int}} = 450\,\text{MPa}$, $\sigma_{\max} = 3000\,\text{MPa}$, $\tau_{\max}^{\text{int}} = 1048\,\text{MPa}$, $\tau_{\max} = 6990\,\text{MPa}$. The impact velocity is $V_1 = 2.5\,\text{m/s}$. The extent of the region shown is 3.0 mm × 3.0 mm. (a) Power law strain rate hardening and $\sigma_0 = 600\,\text{MPa}$ ($t = 9.62\,\mu\text{s}$, $\dot{a}_y = 541\,\text{m/s}$). (b) Enhanced strain rate hardening and $\sigma_0 = 600\,\text{MPa}$ ($t = 7.7\,\mu\text{s}$, $\dot{a}_y = 517\,\text{m/s}$). (c) Power law strain rate hardening and $\sigma_0 = 1000\,\text{MPa}$ ($t = 7.5\,\mu\text{s}$, $\dot{a}_y = 1598\,\text{m/s}$). (d) Enhanced strain rate hardening and $\sigma_0 = 600\,\text{MPa}$ ($t = 7.4\,\mu\text{s}$, $\dot{a}_y = 1777\,\text{m/s}$).

an interface may depend on whether or not the crack speed is fast enough for the material in the near-tip region to enter the enhanced strain rate hardening regime.

For a weaker interface, one where the interface strength is 15 percent of the material cohesive strength, the crack deflects into the interface instead of penetrating it (Figures 10(a) and 10(b)). Interestingly, for the elastic solid the effective crack growth resistance is slightly higher (10 percent – 15 percent) than for straight ahead crack growth, compare Figures 10(c) and 5(b), while for the low flow strength material with power law strain hardening, the effective crack growth resistance is greater for straight ahead crack growth.

Thus, whether or not the effective crack growth resistance is greater for crack deflection into the interface than for straight ahead crack growth or vice versa depends on the plastic flow properties. For a low flow strength material, with power law hardening, the effective crack growth resistance (for a given amount of crack advance) is greater for straight ahead crack growth. On the other hand, for a high strength material there is little difference in the effective crack growth resistance for the two modes of crack propagation and, for the elastic material, crack deflection into the interface gives a higher effective crack growth resistance (Figures 5(b) and 10(c)). It is important to note that the measure of crack advance here is related to the creation of new free surface. When considering the amount of crack growth projected onto the initial crack line, crack deflection enhances the effective crack growth resistance in all cases.

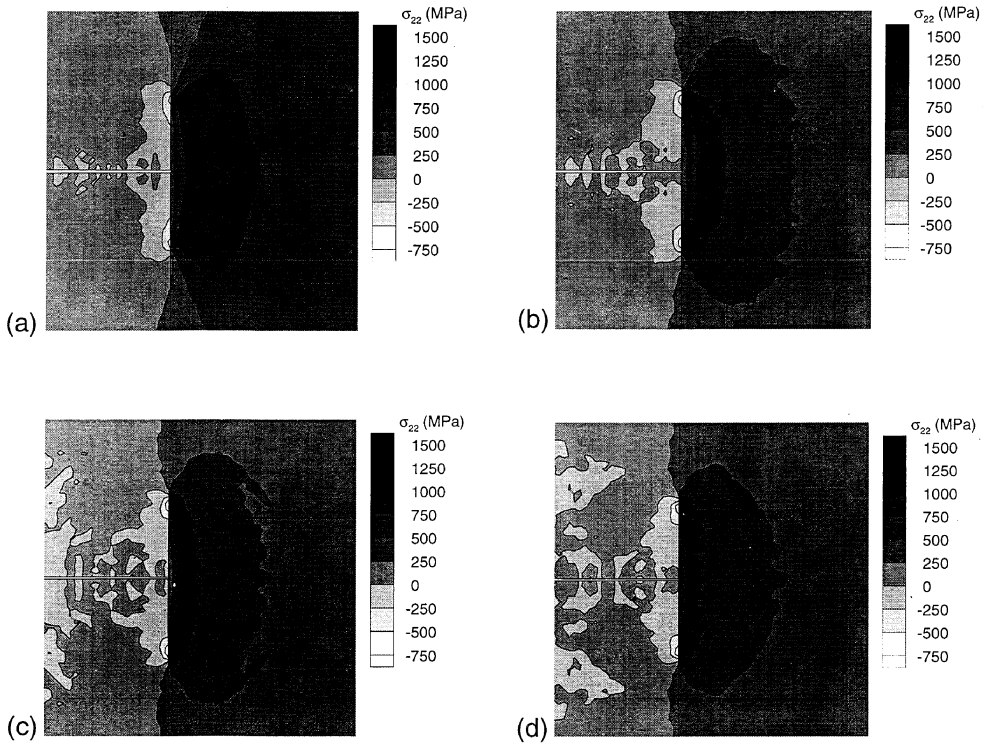

Figure 15. Contours of the physical stress component σ_{22} at $\Delta a_x = 1.2\,\text{mm}$, $\Delta a_y = 0.65\,\text{mm}$ with $\sigma_{\max}^{\text{int}} = 450\,\text{MPa}$, $\sigma_{\max} = 3000\,\text{MPa}$, $\tau_{\max}^{\text{int}} = 1048\,\text{MPa}$, $\tau_{\max} = 6990\,\text{MPa}$. The impact velocity is $V_1 = 2.5\,\text{m/s}$. The extent of the region shown is 3.0 mm × 3.0 mm. (a) Power law strain rate hardening and $\sigma_0 = 600\,\text{MPa}$ ($t = 9.62\,\mu\text{s}$, $\dot{a}_y = 541\,\text{m/s}$). (b) Enhanced strain rate hardening and $\sigma_0 = 600\,\text{MPa}$ ($t = 7.7\,\mu\text{s}$, $\dot{a}_y = 517\,\text{m/s}$). (c) Power law strain rate hardening and $\sigma_0 = 1000\,\text{MPa}$ ($t = 7.5\,\mu\text{s}$, $\dot{a}_y = 1598\,\text{m/s}$). (d) Enhanced strain rate hardening and $\sigma_0 = 1000\,\text{MPa}$ ($t = 7.4\,\mu\text{s}$, $\dot{a}_y = 1777\,\text{m/s}$).

It should be emphasized that the mesh used in the calculations is relatively crude. This precludes consideration of the effect of crack branching in the elastic solid on crack penetration across the interface and on the effective crack growth resistance. Nevertheless, as illustrated in Figure 9, the resolution appears fine enough to give accurate results for straight ahead crack growth. Indeed, the finest mesh resolutions appear to be needed for crack branching studies (Xu and Needleman, 1994) and for resolving large scale plastic flow (Needleman, 1997).

The dissipation accompanying inelastic deformation strongly affects the crack speed and the effective crack growth resistance (Figures 5 and 10), as seen in previous studies, Needleman, (1990b), Tvergaard and Hutchinson, (1992) and Siegmund and Needleman, (1997). The key parameter in this regard, as for homogeneous solids, is the ratio of the material flow strength to the cohesive surface strength. For the range of parameters considered here, the amount of plastic deformation did not change the crack path; for all cases with the strong interface the crack grew straight through the interface, while for all cases with the weak interface the crack was deflected into the interface. There may, however, be circumstances where plastic deformation does make a difference in this regard.

The specific circumstances analyzed here pertain to a crack growing from an iron carbide particle into the surrounding ferrite. If the interface is sufficiently strong, as in Figure 5, and, particularly, if the crack speed is fast enough for enhanced strain rate hardening to come into play, the interface strength essentially plays no role in the course of crack propagation and

analyses of high rate crack growth that neglect this strength, such as in Freund and Hutchinson, (1985) or Siegmund and Needleman, (1997) are relevant. If the interface is weak and the crack deflects into it, the effective crack growth resistance can be quite different. A significant difference between the circumstances analyzed here and those in Siegmund and Needleman, (1997) is that here the crack attains high speeds before the onset of plastic flow. Under the circumstances analyzed in Siegmund and Needleman, (1997), or under quasi-static loading conditions, Tvergaard and Hutchinson, (1992), a ratio of $\sigma_{\max}/\sigma_0 = 5$, would essentially preclude crack growth.

For those features of the crack growth behavior where a comparison can be made with experiment, the present results show very good agreement. One example is the rate of growth of the plastic zone at an arrested crack tip in Figure 8. Another example is provided in Figure 11(b) which shows the crack profile for crack at an interface. There is very good agreement with the crack profile in Shaw et al. (1996), for a crack at an Al_2O_3-Al interface. The crack profiles in Figure 11 are also very similar to those obtained by Finot et al. (1994) in their quasi-static analyses. A direct comparison with experiment is precluded because experiments have focussed on fatigue loading as in Suresh et al. (1992, 1993). However, aspects of the overall behavior, in particular the role of plastic deformation in affecting the crack growth behavior, found in the dynamic calculations here are qualitatively similar to what is observed. It is worth emphasizing that a dynamic formulation may be necessary even for quasi-static loading. As found in Finot et al. (1994), there are parameter ranges of interest where there are no stable equilibrium solutions so that the crack grows dynamically, at least for a while, even under quasi-static loading conditions.

Acknowledgments

We are pleased to acknowledge support from the Air Force Office of Scientific Research under Grant F49620-94-1-0300. T.S. is also grateful for the support provided by Schrödinger Fellowship J00994 – TEC, FWF Vienna, Austria, and by Christian-Doppler-Laboratory for Micromechanics of Materials, Leoben – Vienna, Austria. The computations reported on were carried out on the Cray C90 at the Pittsburgh Supercomputer Center.

References

Ashby, M.F., Blunt, F.J. and Bannister, M. (1989). Flow characteristics of highly constrained metal wires. *Acta Metallurgica* **37**, 1847–1857.

Belytschko, T., Chiapetta, R.L. and Bartel, H.D. (1976). Efficient large scale non-linear transient analysis by finite elements. *International Journal for Numerical Methods in Engineering* **10**, 579–596.

Campbell, J.D. and Ferguson, W.G. (1970). The temperature and strain-rate dependence of the shear strength of mild steel. *Philosophical Magazine* **21**, 63–82.

Cook T.S. and Erdogan, F. (1972). Stresses in bonded materials with a crack perpendicular to the interface. *International Journal of Engineering Science* **10**, 677–697.

Erdogan, F. and Biricikoglu, V. (1973). Two bonded half planes with a crack going through the interface. *International Journal of Engineering Science* **11**, 745–766.

Fields, R.J. and deWit, R. (1990). Plastic zone formation around an arresting crack. *International Journal of Fracture* **42**, 231–238.

Finot, M., Shen, Y.-L., Needleman, A. and Suresh, S. (1994). Micromechanical modeling of reinforcement fracture in particle-reinforced metal-matrix composites. *Metallurgica Transactions A* **25A**, 2403–2420.

Freund, L.B. and Hutchinson, J.W. (1985). High strain-rate crack growth in rate-dependent plastic solids. *Journal of the Mechanics and Physics of Solids* **33**, 169–191.

Goree, J.G. and Venezia, W.A. (1977). Bonded elastic half-planes with an interface crack and a perpendicular intersecting crack that extends into the adjacent material. *International Journal of Engineering Science* **15**, Part I, 1–17; Part II, 19–27.

He, M.-Y. and Hutchinson, J.W. (1989). Crack deflection at an interface between dissimilar elastic materials. *International Journals of Solids Structures* **25**, 1053–1067.

Klopp, R.W., Clifton, R.J. and Shawki, T.G. (1985). Pressure-shear impact and the dynamic plastic response of metals. *Mechanics of Materials* **4**, 375–385.

Krieg, R.D. and Key, S.W. (1973). Transient shell response by numerical time integration. *International Journal for Numerical Methods in Engineering* **7**, 273–286.

Lu, M.-C. and Erdogan, F. (1983). Stress intensity factors in two bonded elastic layers containing cracks perpendicular to and on the interface. *Engineering of Fracture Mechanics* **18**, Part I, 491–506, Part II, 507–528.

Nakamura, T., Shih, C.F. and Freund, L.B. (1985). Computational methods based on an energy integral in dynamic fracture. *International Journal of Fracture* **27**, 229–243.

Needleman, A. (1987). A continuum model for void nucleation by inclusion debonding. *Journal of Applied Mechanics* **54**, 525–531.

Needleman, A. (1990a). An analysis of decohesion along an imperfect interface. *International Journal of Fracture* **42**, 21–40.

Needleman, A. (1990b). An analysis of tensile decohesion along an interface. *Journal of the Mechanics and Physics of Solids* **38**, 289–324.

Needleman, A. (1997). Cohesive surface modeling of fast crack growth. *Computational Mechanics*, in press.

Peirce, D., Shih, C.F. and Needleman, A. (1984). A tangent modulus method for rate dependent solids. *Computers and Structures* **18**, 875–887.

Rice, J.R. (1968). A path independent integral and the approximate analysis of strain concentration by notches and cracks. *Journal of Applied Mechanics* **35**, 379–386.

Shaw, M.C., Clyne, T.W., Cocks, A.C.F., Fleck, N.A. and Pateras, S.K. (1996). Cracking patterns in metal-ceramic laminates: effects of plasticity. *Journal of the Mechanics and Physics of Solids* **44**, 801–821.

Siegmund, T. and Needleman, A. (1997). A numerical study of dynamic crack growth in elastic-viscoplastic solids. *International Journal of Solids Structures* **34**, 769–788.

Suresh, S., Sugimura, Y. and Tschegg, E.K. (1992). The growth of a fatigue crack approaching a perpendicularly-oriented bimaterial interface. *Scripta Metallurgica et Materialia* **27**, 1189–1194.

Suresh, S., Sugimura, Y. and Ogawa, T. (1993). Fatigue cracking in materials with brittle surface-coatings. *Scripta Metallurgica et Materialia* **29**, 237–242.

Sugimura, Y., Lim, P.G., Shih, C.F. and Suresh, S. (1995). Fracture normal to a bi-material interface: effects of plasticity on crack-tip shielding and amplification. *Acta Metallurgica et Materialia* **43**, 1157–1169.

Tvergaard, V. and Hutchinson, J.W. (1992). The relation between crack growth resistance and fracture process parameters in elastic-plastic solids. *Journal of the Mechanics and Physics of Solids* **40**, 1377–1397.

Tvergaard, V. and Hutchinson, J.W. (1996). On the toughness of ductile adhesive joints. *Journal of the Mechanics and Physics of Solids* **44**, 789–800.

Xu, X.-P. and Needleman, A. (1993) Void nucleation by inclusion debonding in a crystal matrix. *Modelling and Simulation in Materials Science and Engineering* **1**, 111–132.

Xu, X.-P. and Needleman, A. (1994). Numerical simulations of fast crack growth in brittle solids. *Journal of the Mechanics and Physics of Solids* **42**, 1397–1434.

Zhou, M., Needleman, A. and Clifton, R.J. (1994). Finite element simulation of shear localization in plate impact. *Journal of the Mechanics and Physics of Solids* **42**, 423–458.